





Improving Stability and Performance of Cesium Mixed Lead Halides for Photovoltaic Applications

YOUSOUF DOUMBIA ^{1,4} AMAL BOUICH ^{1,2,5}
DONAFOLOGO SORO,³ and MARÍ SOUCASE BERNABÉ¹

1.—Institut de Disseny per a la Fabricació i Producció Automatitzada, Universitat Politècnica de València, València, Spain. 2.—Física Aplicada a las Ingenierías Aeronáutica y Naval and Instituto de Energía Solar, Universidad Politécnica de Madrid, Madrid, Spain. 3.—Département des Sciences et Technologie, Ecole Normale Supérieure (ENS) d'Abidjan, Abidjan, Ivory Coast. 4.—e-mail: doumbiyousouf59@yahoo.fr. 5.—e-mail: Ambo1@doctor.upv.es

We have focused on mixed halide perovskite thin films of the formula CsPbX_3 where ($\text{X}_3 = \text{Br}_3, \text{Cl}_3, \text{I}_3, \text{Br}_2\text{Cl}, \text{Br}_2\text{I}, \text{and } \text{I}_2\text{Cl}$) prepared by spin-coating in order to study the effects of partial and total Br substitution. For this purpose, we performed a series of characterizations, including x-ray diffraction, scanning electron microscopy (SEM), atomic force microscopy (AFM), and UV-visible spectroscopy. All the films except CsPbI_2Br showed two characteristic peaks at 2θ angles of 26.80° and 51.80° corresponding to the (111) and (220) crystallographic planes. In the case of CsPbI_2Br , we have the same peaks, but the main ones are located at 15° and 30° for the (100) and (200) planes, respectively. SEM examined the surface morphology of the different mixed lead halide films; the best surface was that of the CsPbBr_2I sample, which is well-coated, dense, with no pinholes and no cracks, and has the largest grain size. In addition, all the mixed halide films showed good absorbance, especially between 600 nm and 900 nm, with band gap values between 1.94 and 2.92 eV.

INTRODUCTION

The energy question is a crucial issue for sustainable development because it is the meeting point of economic, social, and environmental problems. Indeed, almost all of our economic activities are based on energy consumption. However, this energy, composed of fossil resources, poses a major environmental and climatic challenge of global proportions; it is, therefore, crucial to resort to other types of so-called green sources, such as photovoltaic energy.^{1–9} It is in this context that we are interested in the development of perovskite materials for photovoltaic applications. Perovskites have many optoelectronic advantages, creating much excitement around them.^{10–21} Perovskites of

the general formula ABX_3 (A = methylammonium ion MA^+ , formamidinium ion FA^+ or cesium ion Cs^+ ; B = lead ion Pb^{2+} , tin ion Sn^{2+} , and X = Br^- , Cl^- , I^-) have a structure that can be adjusted depending on the ion in the A, B, or X sites. As in our case, several studies have focused on using the cesium cation Cs^+ in the A sites.^{22–27} The inorganic perovskites CsPbX_3 have the advantage over their organic counterparts (MAPbX_3 and FAPbX_3) due to their superior stability and balanced mobility.^{28–30} Among these inorganic CsPbX_3 perovskites, CsPbI_3 is the best layer for photovoltaic applications. Indeed, it shows a lower band gap when the cubic phase is conserved (1.73 eV), whereas CsPbBr_3 ($E_g = 2.22$ eV) has a more stable crystalline structure, and, depending on its morphology, it can retain good carrier mobility, good optoelectronic properties, high photoluminescence quantum yield, and superior stability under humidity and thermal attack.^{22,31–33}

Although perovskites have many benefits, they face some challenges, among which is the stability problem.^{34–36}

(Received August 29, 2022; accepted November 15, 2022;
published online December 8, 2022)

The present work focuses on the mixed halogens CsPbX_3 ($X_3 = \text{Br}_3, \text{I}_3, \text{Br}_2\text{Cl}, \text{Br}_2\text{I}, \text{I}_2\text{Br},$ and I_2Cl) deposited by the one-step spin-coating method in order to enhance their stability and also their performance. The mixed halide samples, fresh and aged, have been investigated to examine their different structural, morphological, and optoelectronics properties, and to understand the degradation process of perovskite thin films.

MATERIALS AND METHODS

Thin Film Manufacture

We prepared our different films using precursors such as CsX (with $X = \text{Br}, \text{Cl},$ and I) and PbX_2 ($X_2 = \text{Br}_2$ and I_2). These precursors were dissolved in dimethylformamide and then deposited by the one-step spin-coating method in an inert medium with a parameter of 4000 rpm for 50 s. As an antisolvent, we used chlorobenzene. After the deposition and 20 min of annealing at 80°C , the films were immediately taken out from the glovebox for characterization, after which they were kept in the ambient environment for 4 weeks, and the aged films were characterized again. The properties of the aged samples have been compared with the fresh samples in the degradation study.

Characterization Techniques

Different characterization techniques are essential for studying the active layers of perovskite-based solar cells. In this sense, they allow us to judge the relevance of our work through the data.

In this study, we have made the following analyses:

- X-ray diffraction (XRD) determines the crystallinity of the thin films and their crystallographic orientations. At the same time, this technique provides information on which layer has the best crystallinity. The range of diffrac-

tion angles 2θ was set between 10° and 60° using a RIGAKU Ultima IV as the apparatus.

- Scanning electron microscopy (SEM; Zeiss ULTRA 55 Excel SEM) was used to obtain the surface images of the different films.
- Atomic force microscopy (AFM) was used to obtain 3D images of the surface and thus the roughness of the layers.
- UV-Visible spectroscopy was used to report on the thin films' optical properties.

RESULTS AND DISCUSSION

Structural Analyses

XRD is the most important technique for analyzing the crystal structure of processed perovskite materials.³⁷⁻³⁹

Indeed, x-rays sent to the material with an angle θ are reflected in part according to Bragg's law: $2d\sin(\theta) = n\lambda$.⁴⁰ In addition, XRD provides structural parameters such as crystallographic orientation and effective lattice strain (ε), which can be calculated using the Scherrer equation from the XRD pattern data:⁴¹

$$\varepsilon = \frac{\beta}{4 \tan(\theta)} - \frac{K\lambda}{D * 4\sin(\theta)} \quad (1)$$

where β is the maximum width at half maximum (FWHM), $K = 0.95$ (Scherrer's constant), λ is the wavelength, D is the crystal size, and θ is the angle of incidence of the x-rays on the material. The lattice dislocation density is evaluated using:

$$\delta = \frac{1}{D^2} \quad (2)$$

These reflected rays depend on the material to which the incident radiation is directed, i.e., the arrangement of the atoms within it and, therefore, the electronic cloud (Fig 1). This response is

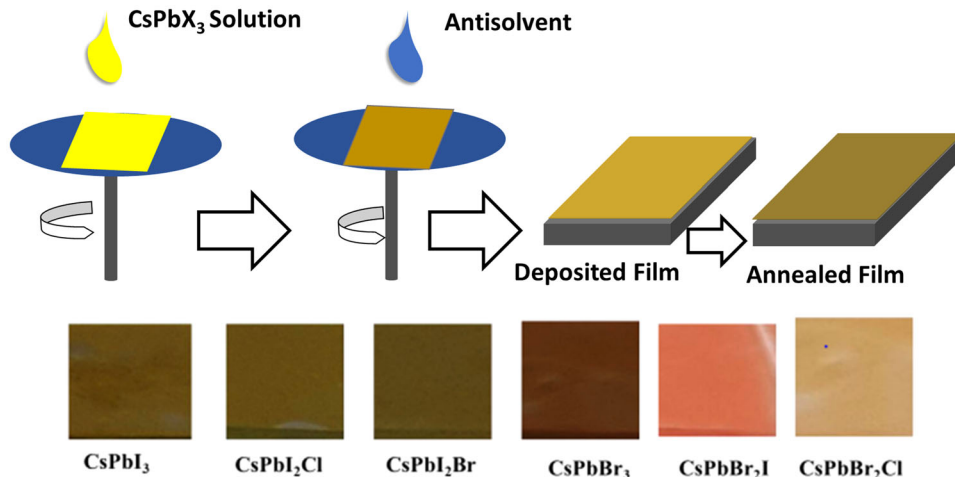


Fig. 1. Procedure and images of CsPbX_3 ($X_3 = \text{Br}_3, \text{I}_3, \text{Br}_2\text{Cl}, \text{Br}_2\text{I}, \text{I}_2\text{Br},$ and I_2Cl) thin films.

captured by a detector and reflected in the appearance of the crystallographic peaks.

In the context of this study, we have the appearance of several peaks (Fig. 2a), the main ones being angles 2θ of 26.80° and 51.80° , corresponding to the (111) and (220) crystallographic planes, respectively, except for the case of the CsPbI_2Br sample, which has its main peaks at 15° and 30° for the (100)

and (200) planes, respectively. The shift in the position of the main peaks of CsPbI_2Br compared to the other samples shows that the crystallographic orientation of CsPbI_2Br is different from the others. This shift in the main peaks of the CsPbI_2Br layer compared to the other layers is probably due to the occupation of the interstitial positions by Br⁻ ions, which are supposed to occupy the sites that the I-

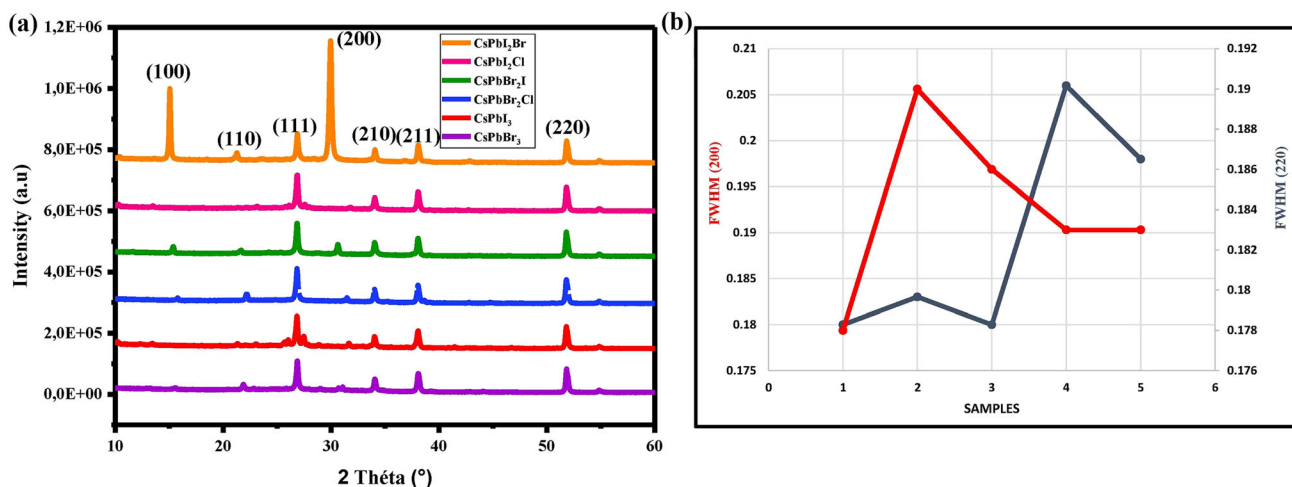


Fig. 2. (a) XRD diagrams of CsPbX_3 ($X_3 = \text{Br}_3, \text{I}_3, \text{Br}_2\text{Cl}, \text{Br}_2\text{I}, \text{I}_2\text{Br},$ and I_2Cl), (b) the FWHM of the (200) and (220) peaks.

Table I. Grain size, dislocation density, and XRD lattice strain of CsPbX_3 thin films

Samples	Grain size (nm)	Dislocation density δ (nm^{-1})	Lattice strain (ϵ)
CsPbBr_3	473	4.47×10^{-6}	0.188
CsPbBr_2Cl	466	4.60×10^{-6}	0.192
CsPbBr_2I	474	4.45×10^{-6}	0.188
CsPbI_3	414	5.83×10^{-6}	0.216
CsPbI_2Cl	431	5.38×10^{-6}	0.207
CsPbI_2Br	353	8.02×10^{-6}	0.188

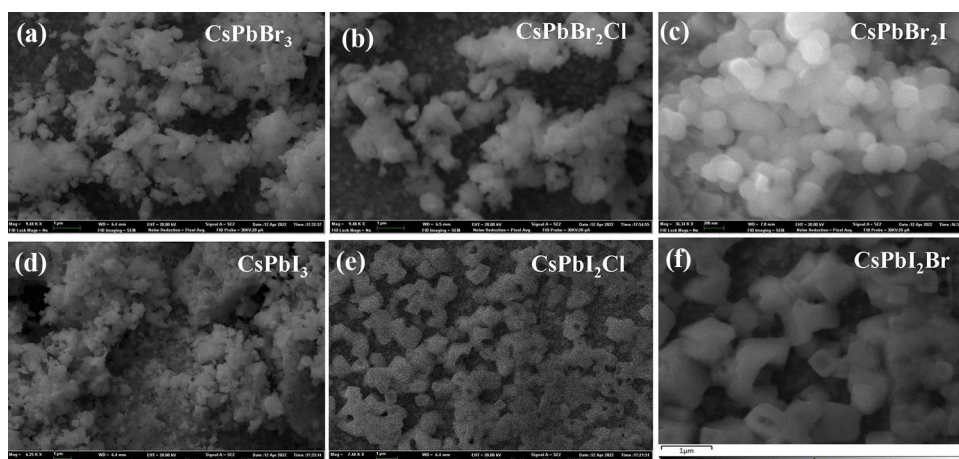


Fig. 3. Surface images of CsPbX_3 with a magnification of $1 \mu\text{m}$ ($X_3 = \text{Br}_3, \text{I}_3, \text{Br}_2\text{Cl}, \text{Br}_2\text{I}, \text{I}_2\text{Br},$ and I_2Cl): (a) CsPbBr_3 , (b) CsPbBr_2Cl , (c) CsPbBr_2I , (d) CsPbI_3 , (e) CsPbI_2Cl , and (f) CsPbI_2Br .

ions they replaced had occupied. This occupation of the interstitial positions changes the crystal structure of the CsPbI_2Br layer, hence the difference.

The intensity of the main peaks for the other five samples is similar, but less than that of CsPbI_2Br , which agrees with the SEM surface images. For CsPbI_2Br , we have a single preferred crystallographic orientation (100), while the other layers have two preferred crystallographic orientations, namely, the (111) and (220) planes. We can conclude that, for the fresh samples, the best crystal structure is the CsPbI_2Br layer. The non-duplication of the peaks shows that we have single-phase layers. The layers' grain size (D) is between 353 and 474 nm (Table I).

Morphology Analysis

The surface morphology of the prepared samples was obtained by SEM. This flow of electrons with adequate energy excites and removes electrons from the material called secondary electrons, which are collected by a detector which gives an image of the sample surface.⁴² The surface images obtained are shown in Fig. 2. We can see that the surfaces have different morphologies. The surfaces are well-coated and dense without pinholes. For the samples CsPbBr_3 , CsPbBr_2Cl , and CsPbI_2Cl (Fig. 3a, b, and e, respectively), the surfaces are not completely covered by the large grains. For the other samples (Fig. 3c, d, and f), we have the appearance of grains of different sizes that cover the whole surface. The

different surfaces are free of cracks and voids, which is good for good surface morphology. The CsPbI_3 film has small grain sizes. From a morphological point of view, we can note that the best surface is that of the CsPbBr_2I and CsPbI_2Br samples, which are well-coated, dense, and with no pinholes or cracks.

Atomic Force Microscopy (AFM)

AFM produces a 3D image of the surface of the thin film with an excellent resolution in the nanometer range.⁴³ It is a fundamental tool for obtaining the topography and, therefore, the surface roughness, which is a critical parameter in the analysis of films for photovoltaic applications. The AFM device has a cantilever with a tip that produces images by scanning the surface. The tip binds to the surface, bending the cantilever, and varying the amount of laser light reflected from the material as it is observed. The force on the cantilever is created by the sample's surface topography.⁴⁴ Indeed, the roughness tells us about the absorption and exciton generation capacity, while considering the spynhole recombination content of electron-hole pairs. Indeed, the rougher the surface, the more the thin film absorbs due to possible reflections and multiple scattering, but at the same time increases the emissivity of the film. The AFM images in Fig. 4 show the roughness of the films produced by the one-step spin-coating method. The roughness of the samples ($5\ \mu\text{m} \times 5\ \mu\text{m}$) varies

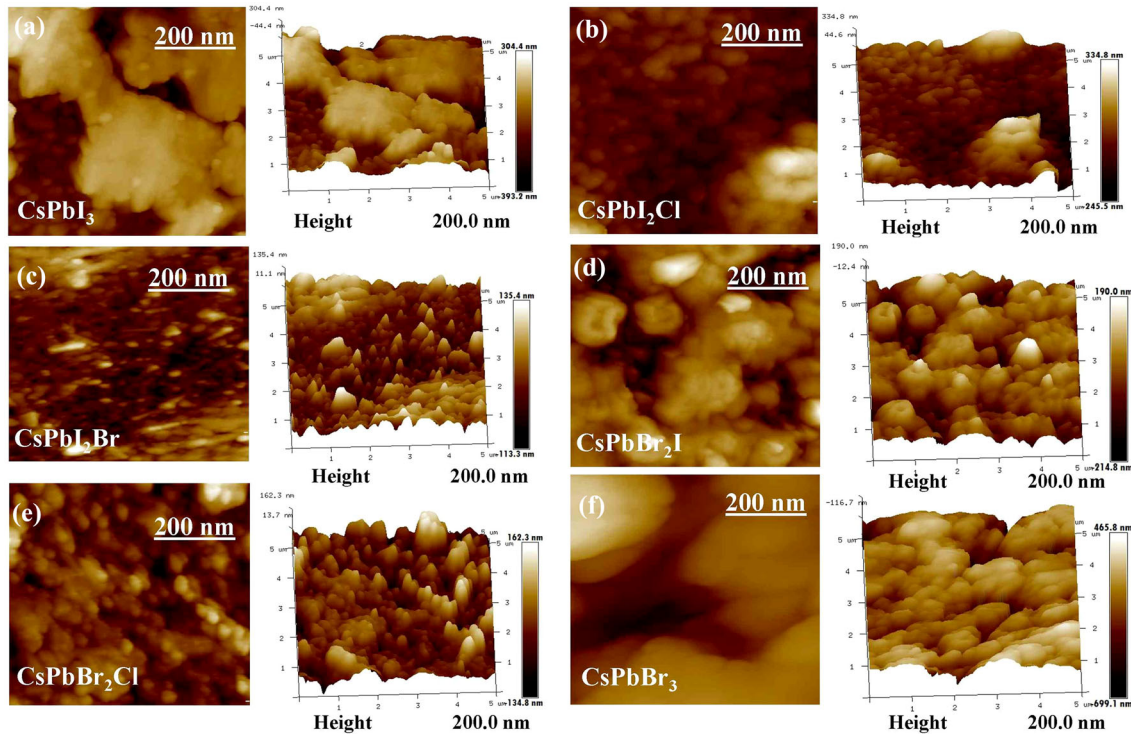


Fig. 4. Two-dimensional (2D) and three-dimensional (3D) AFM images of CsPbX_3 ($X_3 = \text{Br}_3, \text{I}_3, \text{Br}_2\text{Cl}, \text{Br}_2\text{I}, \text{I}_2\text{Br},$ and I_2Cl): (a) CsPbI_3 , (b) CsPbI_2Cl , (c) CsPbI_2Br , (d) CsPbBr_2I , (e) CsPbBr_2Cl , and (f) CsPbBr_3 .

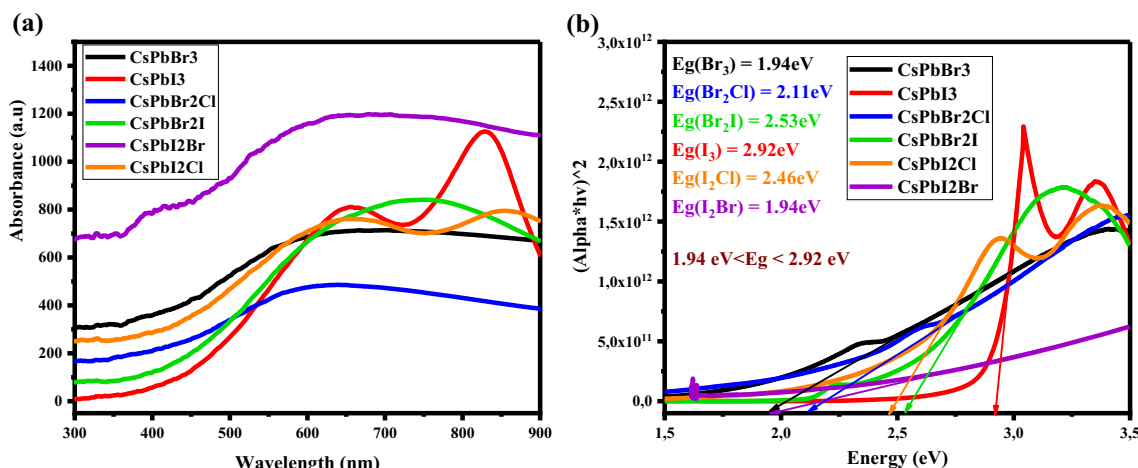


Fig. 5. (a) Absorption curves of the CsPbX₃ (X₃ = Br₃, I₃, Br₂Cl, Br₂I, I₂Br, and I₂Cl) thin films, (b) the band gap of (X₃ = Br₃, I₃, Br₂Cl, Br₂I, I₂Br and I₂Cl).

between 37.5 for CsPbI₂Br nm and 151 nm for CsPbBr₃. In general, as the roughness increases, the band gap also increases. For the roughness of the CsPbX₃ (X₃ = Br₃, I₃, Br₂Cl, Br₂I, I₂Br, and I₂Cl) samples, we have the following values: CsPbI₂Br (R_{\max} = 272 nm); CsPbBr₂Cl (R_{\max} = 274 nm); CsPbI₂Cl (R_{\max} = 518 nm); CsPbBr₂I (R_{\max} = 412 nm); CsPbI₃ (R_{\max} = 553 nm); and CsPbBr₃ (R_{\max} = 1010 nm).

We also notice a return of the band gap to the lowest value of 1.92 eV for the highest roughness, 151 nm (CsPbBr₃), which has a medium absorption. This increase in band gap with roughness probably shows that recombination is related to roughness; as the roughness increases, so does the charge carrier recombination.

UV-Visible Spectroscopy Analysis

UV-visible absorbance is a critical parameter in the characterization of materials used for photovoltaic applications. It should be noted that photovoltaic solar cells are manufactured to capture solar radiation and convert it into electricity. To obtain this absorbance, a beam of light is shone onto the sample. The sample absorbs part of the light, while the other part is transmitted and collected by a detector. Depending on the shift between the intensity of the incident light and the transmitted fringe, we obtain the intensity of the absorbed light. The data from the spectroscopic analysis have been plotted in graphs. Figure 5a shows the absorption plots for the different samples we have constructed. The CsPbI₂Br sample has the highest absorbance over the entire visible spectrum (300–900 nm). For the rest of the films, the absorption order breaks down into two phases, namely from 300 nm to 600 nm for the first phase enhanced by CsPbBr₃, and the lowest absorption corresponds to CsPbI₃. This first phase shows an increase in the absorption coefficient for all the samples. The second phase,

from 600 nm to 900 nm, indicates that the weakest absorption is that of CsPbBr₂Cl, which keeps a relatively constant absorbance, as does CsPbBr₃. The CsPbI₃ and CsPbI₂Cl samples fluctuate, although CsPbI₃ shows the most significant change. The absorption growth from the first phase for the CsPbBr₂I film continues into the second phase, to reach its maximum of around 750 nm before decreasing. The band gap energy is required for photons to create electron-hole pairs. The smaller the band gap, the more electron-hole pairs the material generates, which is required for materials used as active layers in photovoltaic solar cells. The different band gaps of the thin films developed are located between 1.94 eV for CsPbBr₂I and CsPbBr₃ and 2.92 eV for CsPbI₃ (Fig. 5b). Considering the different absorbances and the band gap of the thin films, we can say that the best film in the optical properties is CsPbI₂Br.

DEGRADATION STUDY

After the samples were left in the ambient environment, they were re-characterized to see the effect of the environment. Figure 6 shows the XRD patterns of the fresh layers compared to those obtained for the aged layers. Figure 6a, b, and d (CsPbBr₃, CsPbBr₂Cl, and CsPbI₃, respectively) show a slight decrease in the peaks, whereas, for the CsPbBr₂I, CsPbI₂Cl, and CsPbI₂Br films (Fig. 6-c, e, and f, respectively), there is a strong decrease in peaks, especially for CsPbI₂Br which is literally zero for its main peaks. From the crystallographic point of view, CsPbBr₃ has kept its crystal structure and, consequently, the best layer.

The different comparisons of the absorption coefficients of the fresh and aged samples are shown in Fig. 7. All the samples show a decrease in absorption with a variable spread between them. The decrease is smaller for CsPbBr₂I and CsPbI₂Cl (Fig. 7c and e, respectively) while the CsPbBr₃,

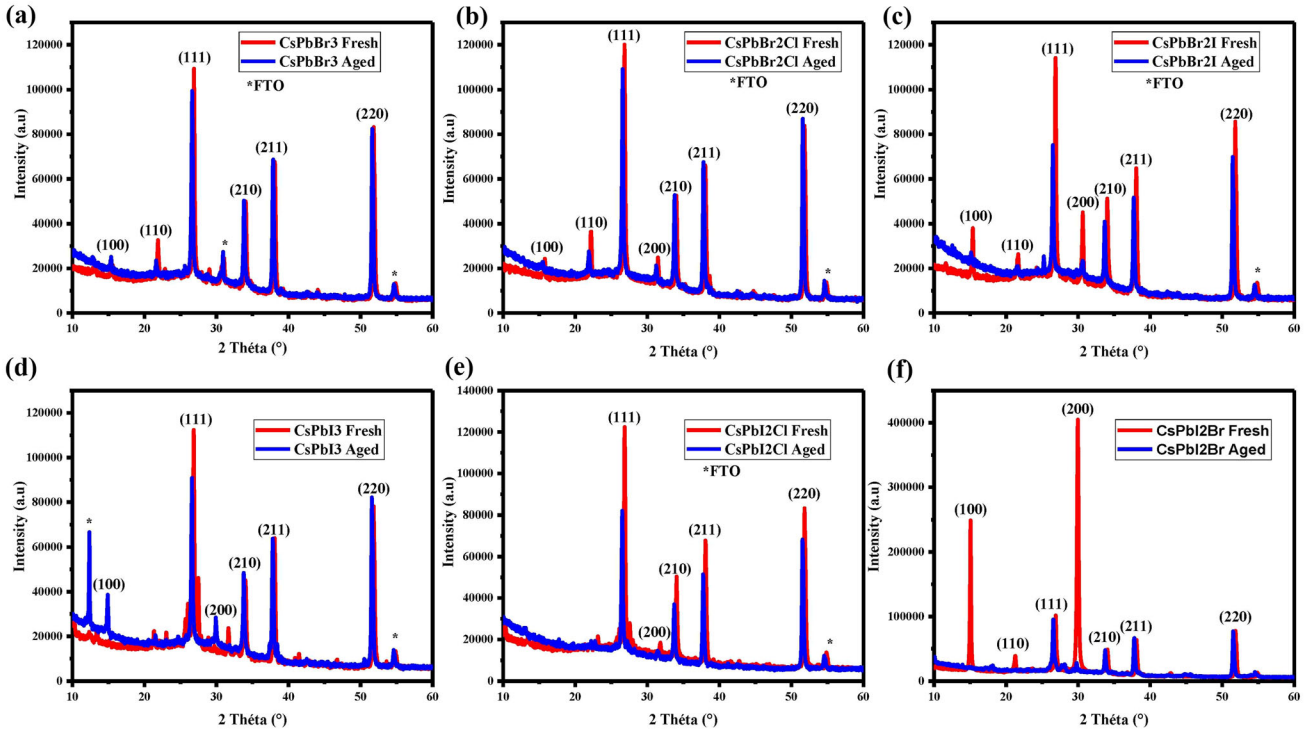


Fig. 6. Comparative XRD plots of fresh and 4-week-old thin films: (a) CsPbBr_3 , (b) CsPbBr_2Cl , (c) CsPbBr_2I , (d) CsPbI_3 , (e) CsPbI_2Cl , and (f) CsPbI_2Br .

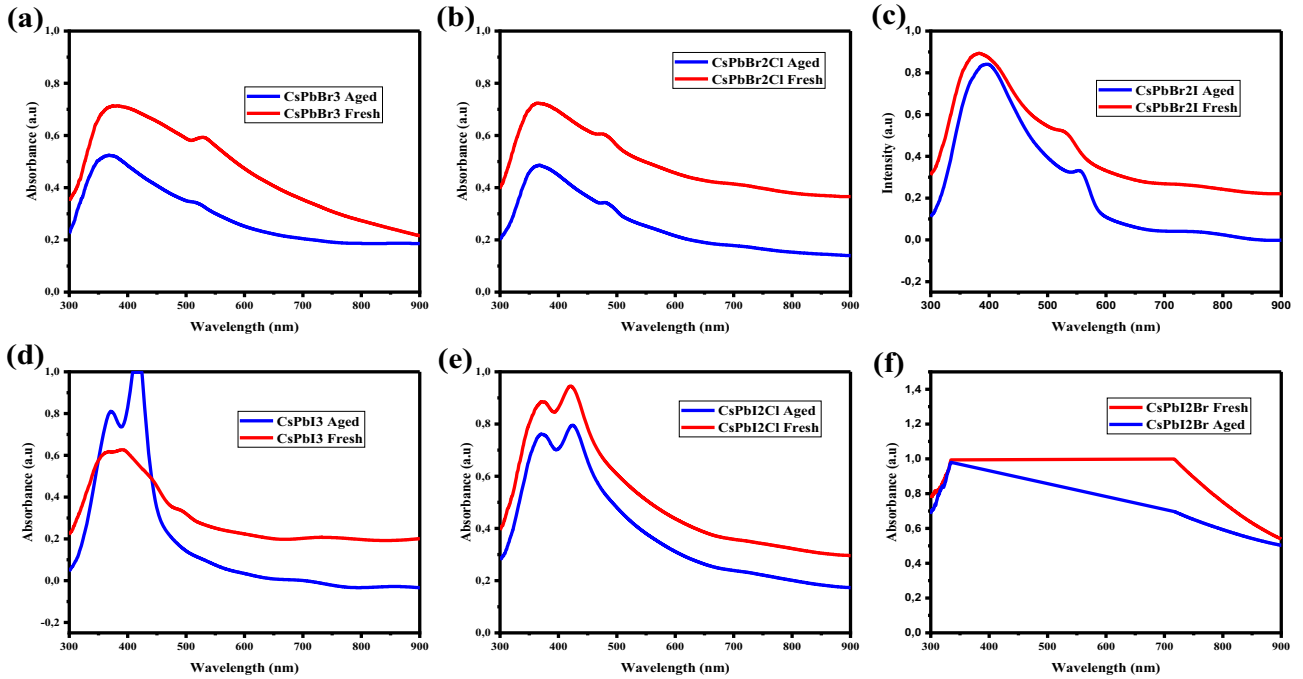


Fig. 7. Absorption curves of fresh and 4-week-old CsPbX_3 ($X_3 = \text{Br}_3, \text{I}_3, \text{Br}_2\text{Cl}, \text{Br}_2\text{I}, \text{I}_2\text{Br}, \text{and I}_2\text{Cl}$): (a) CsPbBr_3 , (b) CsPbBr_2Cl , (c) CsPbBr_2I , (d) CsPbI_3 , (e) CsPbI_2Cl , and (f) CsPbI_2Br .

CsPbI_3 and CsPbI_2Br films (Fig. 7a, d, and f, respectively) have a medium decrease. The largest

decrease is observed for the CsPbBr_2Cl sample (Fig. 7(b)). The layer that best retained its absorption is CsPbI_2Cl .

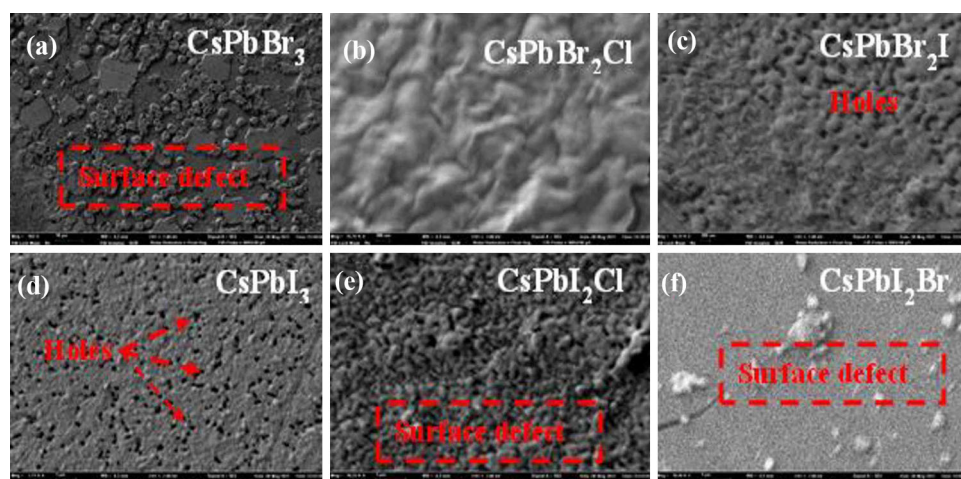


Fig. 8. Surface degradation images of the different samples after four weeks in the ambient environment, CsPbX_3 with a magnification of $1 \mu\text{m}$ ($X_3 = \text{Br}_3, \text{I}_3, \text{Br}_2\text{Cl}, \text{Br}_2\text{I}, \text{I}_2\text{Br},$ and I_2Cl): (a) CsPbBr_3 , (b) CsPbBr_2Cl , (c) CsPbBr_2I , (d) CsPbI_3 , (e) CsPbI_2Cl , and (f) CsPbI_2Br .

The surface degradation images of the thin films are shown in Fig. 8. All the surfaces have degraded to different extents. The CsPbBr_3 , CsPbI_2Br , and CsPbI_2Cl films (Fig. 8a, e, and f, respectively) have a defective surface. The CsPbI_3 film (Fig. 8d) has many pinholes. Although the granules have disappeared from the surface, the CsPbBr_2Cl (Fig. 8b) still has a dense, well-coated surface without cracks. Figure 8c also shows a surface with pinholes.

CONCLUSION

It can be noted that the fresh samples have good surface morphology and variable roughness. XRD analysis revealed the crystallinity of the layers with a crystallographic orientation shift between CsPbI_3 and the other layers. The CsPbI_2Br film has a better surface area and high roughness with a large grain size, which favors light-trapping on the surface.

The prepared films showed relative stability after 1 month (4 weeks) of exposure to the ambient environment. After the different analyses of the fresh and aged films, it can be concluded that the most stable film with good parameters is CsPbBr_3 . These results can help to produce solar cells with maximum efficiency and stability under dark conditions and ambient temperature and humidity.

ACKNOWLEDGEMENTS

Author Youssouf Doumbia acknowledges his grant from Erasmus+ KA 107. Author Amal Bouich acknowledged the post-doctoral contract supported by the RRHH, the Postdoctoral contract Margarita Salas financed with the union European Next Generation EU. This research has been funded by Grant PID2019-107137RB-C22 funded by MCIN/AEI/10.13039/501100011033 and by “ERDF A way of making Europe”.

FUNDING

Open Access funding provided thanks to the CRUE-CSIC agreement with Springer Nature.

CONFLICT OF INTEREST

The authors declare that they have no conflict of interest.

OPEN ACCESS

This article is licensed under a Creative Commons Attribution 4.0 International License, which permits use, sharing, adaptation, distribution and reproduction in any medium or format, as long as you give appropriate credit to the original author(s) and the source, provide a link to the Creative Commons licence, and indicate if changes were made. The images or other third party material in this article are included in the article's Creative Commons licence, unless indicated otherwise in a credit line to the material. If material is not included in the article's Creative Commons licence and your intended use is not permitted by statutory regulation or exceeds the permitted use, you will need to obtain permission directly from the copyright holder. To view a copy of this licence, visit <http://creativecommons.org/licenses/by/4.0/>.

REFERENCES

1. A. Bouich, J. Marí-Guaita, F. Baig, Y. Hameed Khattak, B.M. Soucase, and P. Palacios, *Nanomaterials* 12(17), 3027 (2022).
2. L. Bird, M. Milligan, and D. Lew. National Renewable Energy Lab.(NREL), Golden, CO (United States) (No. NREL/TP-6A20-60451) (2013).
3. D. Gielen, F. Boshell, and D. Saygin, *Nat Mater* 15(2), 117–120 (2016).

4. S. Chu, and A. Majumdar, *Nature* 488(7411), 294–303 (2012).
5. O.A. Al-Shahri, F.B. Ismail, M.A. Hannan, M.H. Lipu, A.Q. Al-Shetwi, R.A. Begum, et al., *J. Clean. Product.* 284, 125465 (2021).
6. A. Bouich, J. Mari-Guaita, B.M. Soucase, and P. Palacios, *Nanomaterials* 12(17), 2901 (2022).
7. A. Tarbi, T. Chtouki, A. Bouich, Y. Elkouari, H. Erguig, A. Migalska-Zalas, and A. Aissat, *Opt. Mater.* 131, 112704 (2022).
8. J. Mari-Guaita, A. Bouich, and B. Mari, *JOM* 74, 1–8 (2022).
9. M.A. Shafi, A. Bouich, K. Fradi, J.M. Guaita, L. Khan, et al. *Optik* 258, 168854 (2022).
10. J. Yu, G. Liu, C. Chen, Y. Li, M. Xu, and T. Wang, et al. *J. Mater. Chem. C* 8(19), 6326–6341 (2020).
11. A. Bouich, J. Mari-Guaita, B. Sahraoui, P. Palacios, and B. Mari, *Energy Res* 10, 840817 (2022).
12. J. Mari-Guaita, A. Bouich, and B. Mari, *Eng. Proc.* 12(1), 1 (2021).
13. Q. Chen, N. De Marco, Y.M. Yang, T.B. Song, C.C. Chen, H. Zhao, et al., *Nano Today* 10(3), 355–396 (2015).
14. N.J. Jeon, H. Na, E.H. Jung, T.Y. Yang, Y.G. Lee, G. Kim, et al. *J. Nature Energy* 3(8), 682–689 (2018).
15. Liu, K., Tian, C., Liang, Y., Luo, Y., Xie, L., & Wei, Z. *Nano Res.* 1–15 (2022).
16. S. Gamliel, and L. Etgar, *RSC Adv* 4(55), 29012–29021 (2014).
17. J.M. Ball, M.M. Lee, A. Hey, and H.J. Snaith, *Energy Environ. Sci.* 6(6), 1739–1743 (2013).
18. J.H. Im, C.R. Lee, J.W. Lee, S.W. Park, and N.G. Park, *Nanoscale* 3(10), 4088–4093 (2011).
19. N.G. Park, *J. Phys. Chem. Lett.* 4(15), 2423–2429 (2013).
20. S.D. Stranks, G.E. Eperon, G. Grancini, C. Menelaou, M.J. Alcocer, T. Leijtens, et al. *Science* 342(6156), 341–344 (2013).
21. G. Xing, N. Mathews, S. Sun, S.S. Lim, Y.M. Lam, M. Grätzel, et al. *Science* 342(6156), 344–347 (2013).
22. A. Bouich, J. Mari-Guaita, A. Bouich, I.G. Pradas, and B. Mari, *Eng. Proc.* 12(1), 81 (2022).
23. S. Bouazizi, W. Thili, A. Bouich, B.M. Soucase, and A. Omri, *Mater. Res. Express* 9(9), 096402 (2022).
24. D. Yang, and D. Huo, *J. Mater. Chem. C* 8(20), 6640–6653 (2020).
25. C.A. López, C. Abia, M.C. Alvarez-Galván, B.K. Hong, M.V. Martínez-Huerta, F. Serrano-Sánchez, et al., *ACS Omega* 5(11), 5931–5938 (2020).
26. J. Deng, J. Li, Z. Yang, and M. Wang, *J. Mater. Chem. C* 7(40), 12415–12440 (2019).
27. P. Ramasamy, D.H. Lim, B. Kim, S.H. Lee, M.S. Lee, and J.S. Lee, *Chem. Commun.* 52(10), 2067–2070 (2016).
28. Y. Gao, Y. Wu, H. Lu, C. Chen, Y. Liu, X. Bai, et al. *Nano Energy* 59, 517–526 (2019).
29. J. Liang, C. Wang, Y. Wang, Z. Xu, Z. Lu, Y. Ma, et al. *J. Am. Chem. Soc.* 138(49), 15829–15832 (2016).
30. J. Liang, X. Han, J.H. Yang, B. Zhang, Q. Fang, J. Zhang, et al. *J. Adv. Mater.* 31(51), 1903448 (2019).
31. X. Li, Y. Tan, H. Lai, S. Li, Y. Chen, S. Li et al. *ACS Appl. Mater. Interfaces* 11(33), 29746–29752 (2019).
32. C.C. Stoumpos, C.D. Malliakas, J.A. Peters, Z. Liu, M. Sebastian, J. Im, et al. *Cryst. Growth Design* 13(7), 2722–2727 (2013).
33. D.N. Dirin, I. Cherniukh, S. Yakunin, Y. Shynkarenko, and M.V. Kovalenko, *Chem. Mater.* 28(23), 8470–8474 (2016).
34. Study and characterization of hybrid perovskites and copper-indium-gallium selenide thin films for tandem solar cells. Bouich, A. (Doctoral dissertation, Universitat Politècnica de València) (2021).
35. S.A.A. Shah, M.H. Sayyad, K. Khan, K. Guo, F. Shen, and J. Sun, et al. *Z. Energies* 13(19), 5092 (2020).
36. J.P. Correa-Baena, M. Saliba, T. Buonassisi, M. Grätzel, A. Abate, and W. Tress, A Hagfeldt, *Science* 358(6364), 739–744 (2017).
37. J. Zheng, M. Zhang, C. F. J. Lau, X. Deng, J. Kim, Q. Ma, et al. *Solar Energy Mater. Solar Cells*, 168, 165–171 (2017).
38. A. Bouich, J. Mari-Guaita, B. M. Soucase, and P. Palacios *Nanomaterials*, 12(17), 2901 (2022).
39. C.R. Dhas, A.J. Christy, R. Venkatesh, K.S. Anuratha, K. Ravichandran, A.M.E. Raj, et al. *Sol. Energy* 157, 58–70 (2017).
40. B.J. Babu, S. Velumani, A. Kassiba, R. Asomoza, J.A. Chavez-Carvayar, and J. Yi, *Mater. Chem. Phys.* 162, 59–68 (2015).
41. A. Bouich, B. Mari, L. Atourki, and S. Ullah, and M.E. Touhami, *JOM* 73(2), 551–557 (2021).
42. A. Dazzi, and C.B. Prater, *AFM-IR: Chem. Rev.;* 117(7):5146–5173 (2017).
43. H. Ezbakhe, and A.A. Donnadieu, *Appl. Res.* 78(2), 607–614 (1983).
44. A. Lrena, F. Millán, G. Pérez, and G. Pinto, *Appl. Surf. Sci.* 187(3–4), 339–346 (2002).

Publisher's Note Springer Nature remains neutral with regard to jurisdictional claims in published maps and institutional affiliations.